Enhanced Energy Deposition of Protons in Aluminium Targets

Weihua JIANG*, Chi ZHANG*, Katsumi MASUGATA* and Kiyoshi YATSUI*

Ion beam interaction with aluminium targets was investigated both experimentally and theoretically. The experiments were performed by using "Plasma Focus Diode" (PFD). The proton energy loss in targets were measured with an improved time-resolvable Thomson-parabola energy spectrometer. Theoretical calculation were made in hydrocode simulations based on free and bound electron stopping terms. With the power density of 0.1 TW/cm² of the ion beam, we observed the enhanced proton energy deposition in the aluminium targets of thickness of 7 μm and 3 μm, which is found to be in reasonable agreement with the calculations.

Key words: beam-target interaction/enhanced stopping power/pulsed ion beam/inertial confinement fusion

I. Introduction

Intense light ion-beam is considered as a hopeful candidate for inertial confinement fusion driver[1]. For studying the physical processes of compressing and heating the target pellet, it is necessary to understand clearly the energy deposition mechanism in high power beam-target interactions. Recently, enhanced energy deposition due to target ionization has been considered of importance in the interactions[2)~7)]. Several authors have reported the enhanced energy deposition with beam -power densities of 0.3~1.4 TW/cm² in different targets[2)~4)]. Furthermore, theoretical works were also carried out to make this phenomenon understandable[5)~7)].

As reported elsewhere, our intense ion beam generator "ETIGO-II" (3 MV, 460 kA, 1.4 TW, 50 ns, 70 kJ) is capable of generating and focusing the ion beam with the power density of ~0.1 TW/cm² by using "Plasma Focus Diode" (PFD)[8)~11)]. We began our studies on enhanced beam-energy deposition with PFD and aluminium targets because PFD generated the ion beams with two-dimensional, line focusing so that the beam power is tightly focused into a small region. In this paper, we first briefly review the present-day research works on enhanced ion stopping power in Sec. II and give the analytical scaling of our experiments in Sec. III. In Sec. IV the diode configuration and the diagnostic methods are summarized, including the details of experimental conditions. We report our experimental results in Sec. V and the simulations of experiment in Sec. VI. We give our concluding remarks in the last section.

Received April 4, 1989

* Laboratory of Beam Technology, Nagaoka University of Technology.

II. Enhanced ion-beam stopping power

We begin with considering an energetic ion moving through a plasma where the collective interaction is not important. In the interested regions of ion energy and plasma temperature, the energy loss rate of the ion can be expressed by:

$$(dE/dx)_{\text{total}} = (dE/dx)_{\text{bound}} + (dE/dx)_{\text{free}} + (dE/dx)_{\text{ion}}, \quad (1)$$

where the first term of the right-hand side is due to the bound electrons of plasma ions or neutral atoms, the second term is due to the free electrons in the plasma, and the third term is due to the ions in the plasma which is usually very small compared to the other two terms. To calculate the energy loss due to bound electrons, one can use the Bethe equation after determining carefully the average ionization potential[12)]. Alternatively, a model called generalized oscillator strength (GOS) was used by McGuire et al[13)] to give the tabulated proton stopping powers for Al^{+n} ($0 \leqq n \leqq 11$). The free-electron stopping power should be described by binary collision

theory[14] within a Debye radius coupled with collective plasma wave excitation outside the Debye radius[15]. Comparison of calculated results of different methods were made by Mehlhorn[5] showing that the simple binary model gives good approximation for the plasma electron stopping power.

Figure 1 shows the 1-MeV proton stopping power of aluminium plasma calculated from eq. (1), where the bound term is cited from McGuire's data and the free term is from Jackson's formula[16]. From Fig. 1 we see that the stopping power is enhanced in the higher temperature region, especially for lower density plasma. Furthermore, the stopping power of plasmas with higher density is much lower than that with lower density because of the lower ionization rate.

Experimentally, the enhanced stopping power was first observed by Young et al[2] in 1982 with the beam power density of 0.3 TW/cm². After that more detailed works were perfomed by Olsen et al[3] with the beam power density of 0.5-1.4 TW/cm². It is noted that the calculation in Ref. 3 gives the aluminium target temperature of less than 50 eV at t = 40 ns, even with beam power density of 1.4 TW/cm².

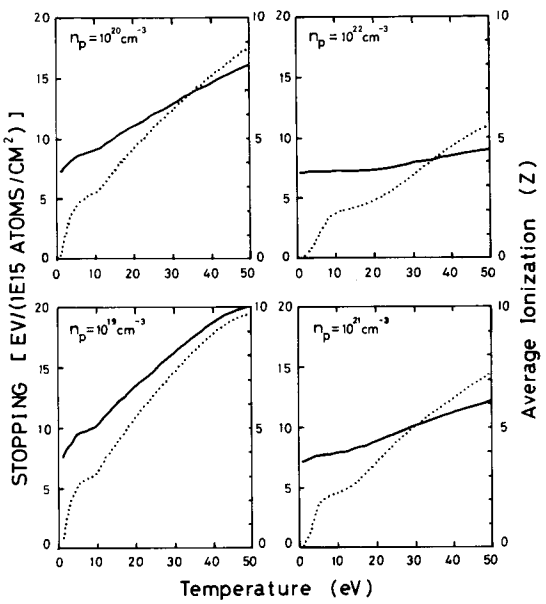

Fig. 1 Proton stopping power of aluminium plasma (solid line) with different temperature and density, together with the average ionization (dashed line).

III. Analytical scaling of PFD experiments

We examined our PFD experimental conditions with the beam power density of 0.1 TW/cm². The analysis was based on the solutions of the following one-demensional hydrodynamic equations:

$$\frac{\partial \rho}{\partial t}+\rho\frac{\partial v}{\partial x}+v\frac{\partial \rho}{\partial x}=0,$$

$$\frac{\partial v}{\partial t}+v\frac{\partial v}{\partial x}+\frac{1}{\rho}\frac{\partial p}{\partial x}=0, \qquad (2)$$

$$\frac{\partial e}{\partial t}+v\frac{\partial e}{\partial x}+\frac{p}{\rho}\frac{\partial v}{\partial x}=\varepsilon(1+\alpha)t^{\alpha},$$

$$p=(\gamma-1)\rho e,$$

where ρ, v, p, e, x, t, and γ are mass density, velocity, pressure, specific energy, length coordinate, time, and isentropic exponent, respectively. The constants ε are α are chosen for convenience so that the term $\varepsilon(1+\alpha)t^{\alpha}$ represents the instantaneous power per unit mass being deposited in the expanding material. For example, when $\alpha=-1$, there is no energy deposition in the target; at $\alpha=0$, the energy deposition rate is constant in time; when $\alpha=1$, the energy deposition rate increases linearly with time.

Combining with simplified initial conditions, the above equations can be solved analytically giving the following solutions:[17]

$$v=\left(\frac{3+\alpha}{2}\right)\frac{x}{t},$$

$$e=\frac{2(1+\alpha)\varepsilon t^{1+\alpha}}{(3+\alpha)\gamma+\alpha-1},$$

$$\rho=M\left(\frac{a}{\pi t^{3+\alpha}}\right)^{1/2}\exp\left(-\frac{ax^2}{t^{3+\alpha}}\right), \qquad (3)$$

where

$$a=\frac{(3+\alpha)\left[(3+\alpha)\gamma+(\alpha-1)\right]}{16(\gamma-1)\varepsilon}.$$

For estimating the deposition term, $\varepsilon(1+\alpha)t^{\alpha}$, we assumed that the ion beam consists of 80% protons and 20% carbon ions. From the waveforms of diode voltage and ion-beam current density (see Fig. 3), we chose α to be 1. Then ε was determined by the average increasing rate (gradient) of total stopping power per unit mass, which was found to be $\sim 1.5\times 10^{28}$ erg/(g·s²) ($t\leqq 30$ ns). Here we did not take the

ionization energy and radiation energy into account. From eq. (3) we found that at t = 30 ns, the target temperature is evaluated for ~30 eV and the plasma density ranges from 10^{19} to 10^{20} cm^{-3}. Therefore, according to Fig. 1 we expect the enhancement ratio (defined as the ratio of energy loss in plasma to that in cold-target) to be 1.5~2.0 for aluminium target.

IV. Experimental arrangement and diagnostics

PFD is a new type of self-magnetically insulated, ion-beam diode.[8] The structure of PFD is shown in Fig. 2 together with the ion energy spectrometer. Basically, it consists of a pair of coaxial cylindrical electrodes with diameters of 35 mm (anode) and 22 mm (cathode), respectively. The axial length is 40 mm. Epoxy was used as the ion source for the flashboard anode. The ion beam generated from the anode is two-dimensionally focused (line focusing) toward the central axis through the perforated cathode which is drilled with holes (1 mm in diameter) with a transparency of ~40%.

The typical waveforms of diode voltage, diode current and ion-beam current density are shown in Fig. 3. The voltage waveform shown in Fig. 3 has been inductively corrected (noted as V_d^*). It peaks at about 1.5 MV and the peak current value is about 150 kA. The ion-current density was measured by a biased-ion collector (BIC) at the position of r = 11 mm and z = 5 mm. The ion-beam power density at the focus point was estimated by using the ion current density on anode surface (J_a) determined by BIC and the focusing radius r* measured by Rutherford-scattering pinhole camera :[8]

$$P_f = (r_a/r^*)J_a V_d^*.$$

At different positions along the axis of PFD (z direction), r* was measured to be 0.18~0.25 mm, while the J_a was 1.4~1.9 kA/cm², then P_f was calculated as ~0.1 TW/cm². With this method, the uncertainty for P_f which mainly comes from Δr^* was found to be ~30%.

In PFD, the target foil was inserted on the focusing line of the diode with an angle of 45° to the axis, which was also used as the Rutherford-scattering foil. As shown in Fig. 2, ions scattered by the target enter the first pinhole after penetrating the target foil with an effective length of $\sqrt{2}d$, where d is the target thickness.

The scattered ion beam is collimated by the pinholes and then analyzed by a Thomson-parabola spectrometer (TPS), the structure of which is also shown in Fig. 2. Principally, it is the same as the conventional Thomson-parabola spectrometer.[3] In order to obtain a smaller spot of the beamlet, we have located the second pinhole of the collimator

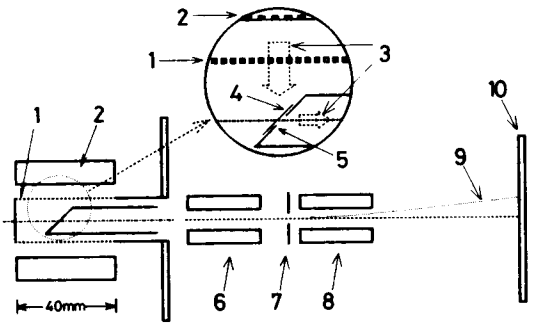

Fig. 2 Schematic of the PFD and TPS. 1. cathode, 2. anode, 3. ion beam, 4. scatterer, 5. first pinhole, 6. magnetic deflector, 7. second pinhole, 8. electric deflector, 9. typical proton orbit, 10. detector (CR-39).

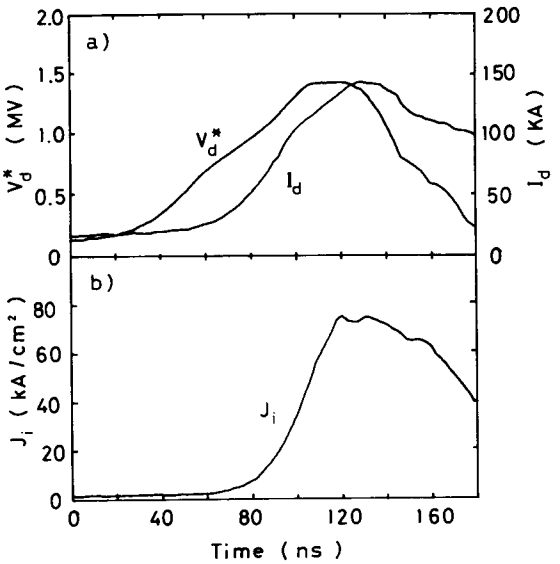

Fig. 3 Waveforms of (a) V_d^* and I_d and (b) J_i, where J_i was detemined by focal radius r* and ion-beam current density measured at r = 11 mm and z = 5 mm with BIC.

between the magnetic and the electric deflectors. As a result, the time- and energy-resolutions are significantly improved. We used an appropriate time-varying electric field to carry out the time-resolved detection of the ion energy. Experimentally, the deflecting electric field was in the oscillating waveform with the peak value of 25 kV/cm and the period of ~300 ns, which is generated by a C-L oscillator triggered by the delayed pulser. The intensity of the magnetic field generated by a permanent magnet is 0.78 T. Both pinholes of the collimator have the diamter of 0.6 mm. The ion traces are recorded on a CR-39 track-recording plastic film which can be read out after etching in a solution of sodium hydroxide for at least two hours. From the traces of the ions, we calculated their energy and time dependence after taking the time of flight into account.

In order to determine the proton energy loss correctly, we must find the incident energy of the protons. We did this in two respects: first we made the inductive correction of the voltage waveform very carefully with accurate calculation of the total inductance, and then tested the corrected waveform by using a thin gold scatterer, since the energy loss of protons in this scatterer is very small. Then the proton energy loss was calculated from the difference between the detected energy value and V_d^* at the correspondent instant. The scatterer is made of gold of 0.22 μm thick coated on a 2-μm mylar film.

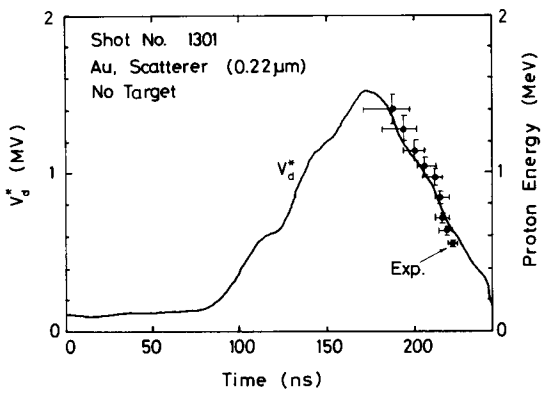

Fig. 4 Experimental result of energy spectrum of protons in the absence of target.

V. Experimental results

Figure 4 shows the experimental results of energy spectrum of the protons in the absence of a target, where the energy loss in the scatterer has been considered. The proton energy spectrum is found to be in good agreement with the waveform of V_d^*.

Proton energy loss measurement has been carried out for aluminium targets, the data of which is presented in Fig. 5. In Fig. 5, for comparison, we also plotted the proton energy calculated from the waveform of V_d^* subtracted the cold-target energy loss. Here we have used the data given by Andersen et al.[12] The energy loss due to elastic scattering of protons has been considered in Fig. 5.

The error bar shown in Figs. 4 and 5 is mainly

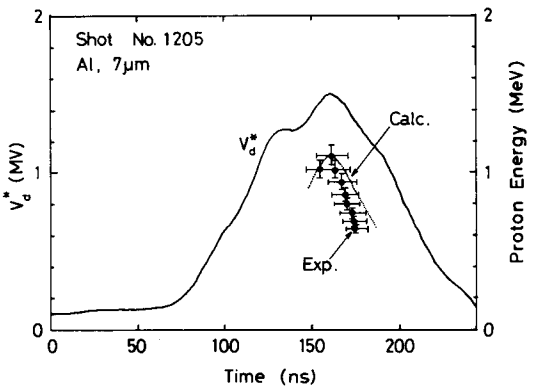

Figure 5(a)

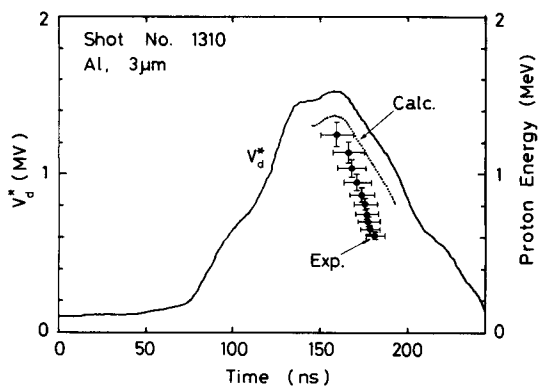

Figure 5(b)

Fig. 5 Results of experimental and calculated (cold-target) proton energy spectrum together with the waveform of V_d^*. (a) 7-μm Al, (b) 3-μm Al.

determined from the uncertainty caused by the sizes of the two pinholes.

Figure 5 (a) and 5 (b) illustrates the similar data for 7- and 3-μm aluminium, respectively. From these figures, we can clearly see the enhanced energy loss which is indicated by the difference between E_{exp} and E_{calc}.

VI. Simulation Results

A one-dimensional hydrodynamic calculation code was used to simulate the expansion procedure of aluminium foils. The hydrodynamic equations are similar to those of section III, while the equation of conservation of energy includes energy deposition term (ε_d), ionization term (ε_i) and energy flux term (ε_f):

$$\frac{\partial e}{\partial t}+v\frac{\partial e}{\partial x}+\frac{p\partial v}{\rho\partial x}=\varepsilon_d+\varepsilon_i+\varepsilon_f. \qquad (4)$$

The ion beam is supposed to be parallel to the incident angle of 45°. Beam composition is 80% protons and 20% carbon ions as assumed before. For different shots the same beam characterization was used, where the ion-beam current density is as shown in Fig. 3, and the individual voltage histories were used. The stopping power of bound electrons was calculated using the tabulated data of McGuire et al[13] by means of fitting. Free electron stopping power was calculated by simple binary collision model[5]. The population of each ionization degree was calculated using the Saha equation under the assumption of local thermodynamic equilibrium (LTE). The energy flux term (ε_f) of eq. (4) involves radiation transport and electron thermal conduction. Radiation heat transfer was treated in the conduction approximation and the radiation conductivity was calculated according to Ref. 18. The electron conductivity was calculated according to Ref. 14. Boundary conditions were determined by blackbody radiation.

Figure 6 shows the simulation results for (a) 7-μm and (b) 3-μm aluminium together with the experimental data. The enhancement ratios are compared in Fig. 7. Figure 8 shows the time histories of temperature, density and average ioniza-

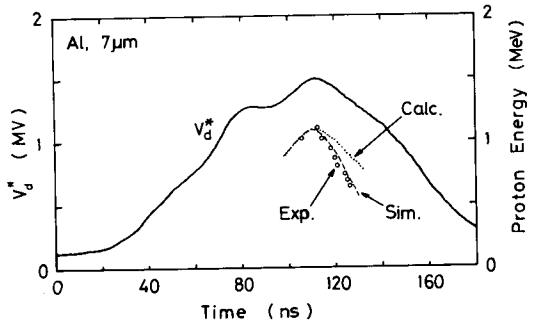

Figure 6(a)

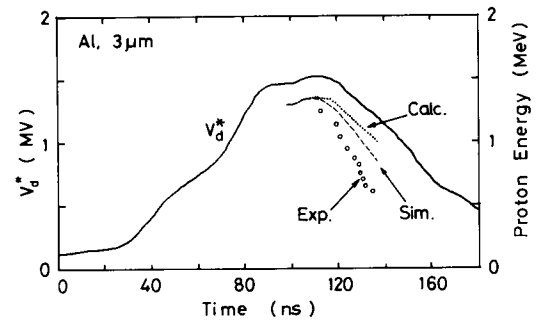

Figure 6(b)

Fig. 6 Simulation results of proton energy loss (dashed line) in comparison with experimental results (circle) and cold target energy loss (dotted line). (a) 7-μm Al, (b) 3-μm Al.

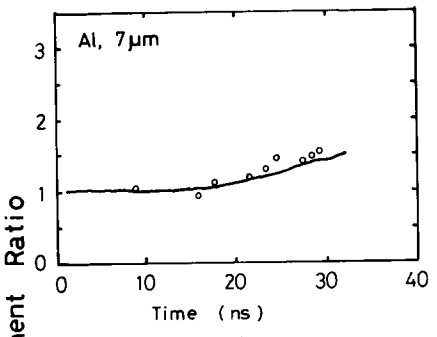

Figure 7(a)

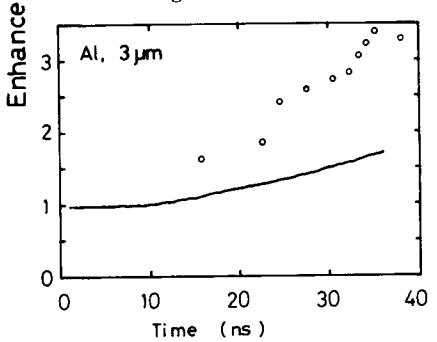

Figure 7(b)

Fig. 7 Simulation results of enhancement ratio of energy deposition (denotation are as for Fig. 6).

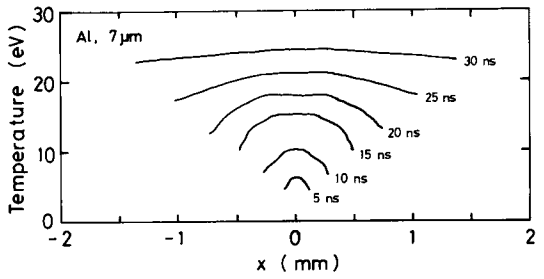

Figure 8(a)

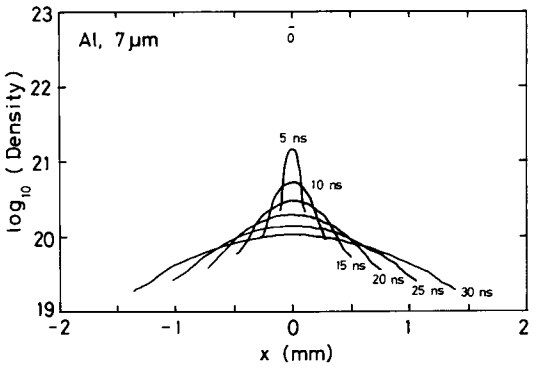

Figure 8(b)

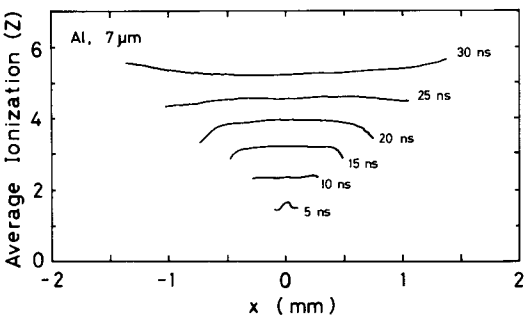

Figure 8(c)

Fig. 8 Simulation results of target a) temperature, b) density and c) average ionizaion, for 7-μm aluminium.

tion for reference as calculated results of 7-μm aluminium.

Comparing the experimental results with the calculation results, we see that our theoretical model agrees fairly well with the experiments for 7-μm aluminium, but differs for 3-μm aluminium. Our considerations are as follows. We have experimental uncertainty in two respects: One is the system error that is shown as error bar in Fig. 5. As described in Sec. V, the error mainly stems from the collimator. Therefore, it differes with the shots. The another is uncertainty of the energy of incident protons, which is caused by the inconsistency of the detected V_d* with the real incident energy of protons. Futhermore, for 3-μm aluminium, the cold-target energy loss is very small so that a small difference in output proton energy causes a big difference in the enhancement ratio. As a result, the error of 3-μm aluminium seems to be greater than that of 7-μm, and hence more detailed studies should be carried out.

VII. Concluding remarks

From the above studies, we conclude as follows: 1) By using PFD (beam power density of 0.1 TW/cm^2), the enhanced proton energy deposition was observed in aluminium targets. 2) According to hydrocode results, the target in PFD can be heated to the temperature of ~30 eV and electron density of ~10^{21}/cm^3. 3) Theoretical model incorporating free and bound electron stopping terms is suitable to describe the energy loss of protons in aluminium plasma.

Acknowledgements

This work was partly supported by a Grant-in-Aid from the Ministry of Education, Science and Culture of Japan. Experimental support given by Mr. Hironobu Isobe and Mr. Norihide Yumino of Laboratory of Beam Technology are acknowledged with thanks.

References

1) S. Humphries, Jr., Nuclear Fusion, **20**, 1549 (1980).
2) F.C. Young, D. Mosher, S.J. Stephanakis, S.A. Goldstein and T.A. Mehlhorn, Phys. Rev. Lett. **49**, 549 (1982).
3) J.N. Olsen, T.A. Mehlhorn, J. Maenchen and D.J. Johnson, J. Appl. Phys. **58**, 2958 (1985).
4) H. Bluhm, B. Goel, P. Hoppe, H.U. Karow and D. Rusch, Proceedings of 7th International Conference on High-Power Particle Beams, Karlsruhe, West Germany, **I**, 381 (1988).
5) T.A. Mehlhorn, J. Appl. Phys. **52**, 6522 (1981).
6) E. Nardi, E. Peleg and Z. Zinamon, Appl. phys. Lett. **39**, 46 (1981).
7) K.A. Long and N.A. Tahir, Phys. Fluids, **29**, 4204 (1986).
8) K. Yatsui, K. Masugata and S. Kawata, Proceedings of

8th International Workshop on Laser Interaction and Related Plasma Phenomena, Montery, California, USA (1987).

9) K. Yatsui, Y. Shimotori, H. Isobe, W. Jiang and K. Masugata, Proceedings of 12th International Conference on Plasma Physics and Controlled Nuclear Fusion Research, Nice, France, IAEA-CN-50/B-4-2 (1988).

10) K. Yatsui, K. Masugata, Y. Shimotori, K. Imanari, M. Murayama, M. Yokoyama and T. Takaai, Proceedings of 7th International Conference on High-Power Particle Beams, Karlsruhe, West Germany, **I**, 522 (1988).

11) K. Masugata, H. Isobe, K. Aga, M. Matsumoto, S. Kawata, W. Jiang and K. Yatsui, Laser and Particle Beams, **7**, 287 (1989).

12) H.H. Andersen and J.F. Ziegler, Hydrogen-Stopping Powers and Ranges in All Elements (Pergamon, New York, 1977).

13) E.J. McGuire, J.M. Peek and L.C. Pitchford, Phys. Rev. A26, 1318 (1982).

14) L. Spitzer, Jr., Physics of Fully Ionized Gases (Wiley, New York, 1960), p. 128.

15) D. Pines and D. Bohm, Phys. Rev. 85, 338 (1952).

16) J.D. Jackson, Classical Electrodynamics (Wiley, New York, 1975), p. 643.

17) A.V. Farnsworth, Jr., Phys. Fluids, **22**, 859 (1979).

18) Ya.B. Zeldovich and Yu.P. Raizer, Physics of Shock Waves and High Temperature Phenomena (Academic, New York, 1967), Vol. I, Chap. II ; Vol. II, Chap. X.